



Intrinsic layered defects in solid-state electrolyte $\text{Li}_{0.33}\text{La}_{0.56}\text{TiO}_3$

Shang Peng^{a,b}, Yongjin Chen^b, Boya Wang^{c,d}, Xuefeng Zhou^b, Haijun Yu^{c,d},
Jianbo Wang^{a,***}, Wenge Yang^{b,**}, Xiang Gao^{b,*}

^a School of Physics and Technology, Center for Electron Microscopy, MOE Key Laboratory of Artificial Micro- and Nano-structures, and Institute for Advanced Studies, Wuhan University, Wuhan, Hubei, 430072, PR China

^b Center for High Pressure Science and Technology Advanced Research (HPSTAR), Beijing, 100094, PR China

^c Institute of Advanced Battery Materials and Devices, Faculty of Materials and Manufacturing, Beijing University of Technology, Beijing, 100124, PR China

^d Key Laboratory of Advanced Functional Materials, Ministry of Education, Beijing University of Technology, Beijing, 100124, PR China



HPSTAR
1571-2022

ARTICLE INFO

Article history:

Received 15 September 2021

Received in revised form

21 November 2021

Accepted 23 November 2021

Available online 26 November 2021

Keywords:

Perovskite

Stacking faults

Domain formation mechanism

Cation segregation

ABSTRACT

Perovskite $\text{La}_{2/3-x}\text{Li}_x\text{TiO}_3$ is a typical solid-state electrolyte for all-solid-state lithium-ion batteries. The material system has been intensively studied because of its high bulk ionic conductivity and great efforts have been devoted to explore the structure-property relationship and further enhancement of the property through structural modification. However, the microstructure and its critical role in the ionic conductivity of $\text{La}_{2/3-x}\text{Li}_x\text{TiO}_3$ remain scarce in the literature. In this work, based on an in-depth study via aberration-corrected scanning transmission electron microscopy and first-principles calculation, we report the formation of intrinsic layered defects which act as Li-ion-blocking layers. By forming enclosed loops scaled from nanometers to micrometers, the layered defects are found to occur uniformly at domain boundaries. The results provide insights into the influence of these layered defects on Li-ion transport, as well as their formation mechanism as a result of phase transition at high sintering temperatures, paving the way to develop novel perovskite solid-state electrolytes via microstructure engineering.

© 2021 Elsevier Ltd. All rights reserved.

1. Introduction

Lithium-ion batteries have been widely used in portable electronic devices and electric vehicles [1–3]. Conventional lithium-ion batteries containing flammable organic liquid electrolytes give rise to serious safety problems. All-solid-state batteries based on non-flammable inorganic solid-state electrolytes (SSEs) are expected to greatly improve the safety performance, offering high chemical and thermal stability, absence of leakage, and high resistance to shocks and vibrations [4–6]. Among the potential SSE materials, sulfide-based SSEs show high Li-ion conductivity, which is comparable with liquid electrolytes. However, sulfide-based SSEs usually suffer from electrochemical and chemical stable problems during long-term cycling [2,3]. Oxide SSEs have attracted considerable attention because these materials show high stability for high voltage battery applications and are relatively stable in air than sulfide SSEs. Perovskite $\text{La}_{2/3-x}\text{Li}_x\text{TiO}_3$ (LLTO) is one of the

promising oxide SSEs for all-solid-state batteries, which show the highest bulk Li-ion conductivity compared with other oxide SSEs such as $\text{Li}_7\text{La}_3\text{Zr}_2\text{O}_{12}$ and $\text{Li}_{1.3}\text{Al}_{0.3}\text{Ti}_{1.7}(\text{PO}_4)_3$ [2–4].

Depending on the Li content, LLTO exhibits either a tetragonal ($x \geq 0.1$) or an orthorhombic ($x < 0.1$) structure at ambient temperature [7–11]. In common, the two phases have a layered structure consisting of alternate stacking of La-rich and La-poor (001) atom planes along the *c*-axis [12–14]. Whereas at a high temperature ($> 1,200^\circ\text{C}$), LLTO shows a cubic crystal symmetry with a space group of $Pm\bar{3}m$ [15–17]. Although LLTO shows a high bulk ionic conductivity of more than $1 \times 10^{-3} \text{ S cm}^{-1}$ at ambient temperature [8], the overall ionic conductivity is relatively low, ranging between 10^{-4} and $10^{-5} \text{ S cm}^{-1}$, which has been an obstacle to its application [18,19]. Based on electrochemical impedance spectroscopy (EIS) measurements [8,20], reasons for the low overall conductivity were ascribed to the boundaries and interfaces. Recently, Gao et al. [21] uncovered that crystalline LLTO contains large numbers of 90° -rotation domain boundaries (DBs) and a much less common antiphase-type boundary (APB). It was found that 90° DBs are subject to considerable lattice strain and significant segregation of La atoms, which serve to block lithium migration [21]. In particular, first-principles calculations further suggested that the bulk ionic conductivity of LLTO could

* Corresponding author.

** Corresponding author.

*** Corresponding author.

E-mail addresses: wang@whu.edu.cn (J. Wang), yangwg@hpstar.ac.cn (W. Yang), xiang.gao@hpstar.ac.cn (X. Gao).

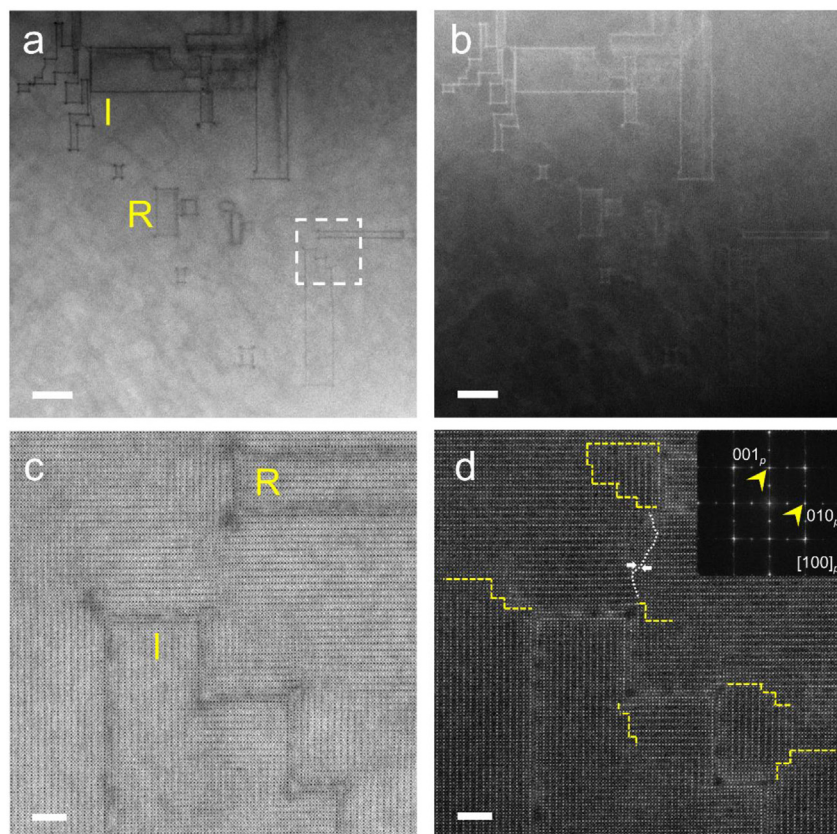


Fig. 1. The morphology of enclosed loops in LLTO. (a) BF and (b) LAADF images show the two types of enclosed loops, irregular and rectangle separate, indicated as red I and R, respectively. The enlarged high-resolution (c) BF and (d) LAADF images of the white-labeled rectangle region in (a). The inset in (d) is the corresponding Fast Fourier Transfer (FFT) pattern of (d). 90° DBs marked as a yellow dashed line. An antiphase DB is marked as a dashed white curve, and the two opposing arrows show the lattice glide of $1/2[001]_p$ between two domains. The scale bars in (a) (b) and (c) (d) are 50 nm and 5 nm, respectively. LAADF, low-angle annular dark field; DB, domain boundary; LLTO, $\text{La}_{2/3-x}\text{Li}_x\text{TiO}_3$.

be up to three orders of magnitude higher without these 90° DBs [22]. Zhu et al. [23] reported that a termed ‘single-atom-layer-trap’ forms enclosed loops, and thus the enclosed volumes could not participate in the overall ionic transport, degrading the total conductivity. These recent works enable novel insights into the varied microstructures, which affect significantly the Li-ion conduction in LLTO. In other words, engineering intrinsic microstructures (DBs, lattice defects) could be one effective way to improve further the ionic conductivity of LLTO. Nevertheless, knowledge for the formation of the intrinsically existed defects, e.g. dislocations, stacking faults, and DBs, remains scarce in the literature.

In this work, we use the advanced aberration-corrected scanning transmission electron microscopy (STEM) techniques and first-principles calculations to explore the structure and formation mechanism of intrinsic lattice defects in crystalline LLTO and illustrate their influence on the ionic conductivity property in this material. For the first time, we propose a phase transition induced kinetic process to depict the domain growth and its relation to the formation of the layered defects at DBs.

2. Results and discussion

The LLTO ceramic samples used in this work were synthesized by solid-state reaction [21,23]. The composition was examined by the inductively coupled plasma (ICP) spectroscopy, showing a molar ratio of Li: La: Ti, that is nearly identical to the nominal

stoichiometry 0.33: 0.56: 1. The diameter and thickness of the ceramic pellets were 10.2 mm and 1.1 mm, respectively. The relative density was calculated at 94.5%. Scanning electron microscopy (SEM) image indicated that the grain size was about 1–5 μm (Fig. S1). XRD analysis (Fig. S2) suggested that the obtained ceramic has tetragonal crystal symmetry, in consistence with previous results [24,25]. Electrochemical impedance spectroscopy measurement indicated that the bulk, grain boundary, and overall ionic conductivity were $1.05 \times 10^{-3} \text{ S cm}^{-1}$, $3.44 \times 10^{-5} \text{ S cm}^{-1}$, and $3.33 \times 10^{-5} \text{ S cm}^{-1}$, respectively (Fig. S3).

Fig. 1 shows the enclosed loops and DBs images of the LLTO sample along the $[100]_p$ direction (the subscript p refers to the primitive perovskite unit cell). Fig. 1a shows the low magnification ABF image of the two types of enclosed loops, frequently observed irregular enclosed loop (hereafter named I loop) and much less common separate rectangle enclosed loop (hereafter named R loop). The loops regions with brighter contrast in the low-angle annular dark field (LAADF) image are displayed in Fig. 1b. The LAADF contrast is sensitive to any lattice distortion that leads to increased thermal diffuse scattering of transmitted electrons [26]; therefore, the brighter contrast of these loops than that of bulk indicates the existence of severe lattice distortion in LLTO. Weak-beam dark-field TEM images (Fig. S4) reveal that these loops are consist of 90° -oriented stacking faults. Fig. 1c and d show the enlarged atomic-resolved ABF and LAADF images of the R loop and I loop, and the stacking fault layers are either perpendicular or parallel to the $(001)_p$ plane.

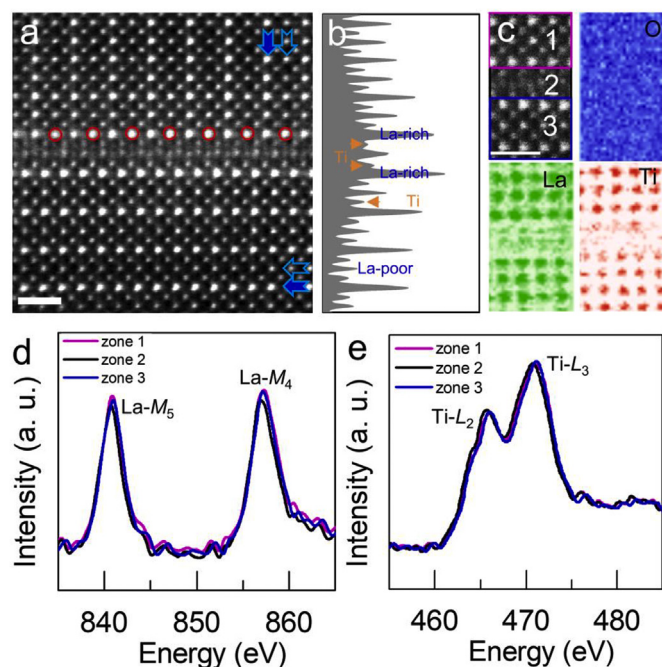


Fig. 2. Atom structure analysis of the stacking fault. (a) HAADF and (b) corresponding integrated intensity profile along the horizontal direction. The La-rich and La-poor layer orientation were indicated by solid and empty arrows. Red circles indicated the La-rich columns located at the La-poor layers caused by the neighboring defect layer. (c) Atomic resolution HAADF image and corresponding element distribution roughly revealed by EELS mapping. EELS spectra of (d) La-M and (e) Ti-L were taken from the three zones in (c). HAADF, high-angle annular dark field; EELS, electron energy loss spectroscopy.

Detailed STEM analysis was carried out to unravel the structure and chemistry of the stacking fault layer (Fig. 2). The high-angle annular dark field (HAADF) image in Fig. 2a displays a typically single stacking fault along the $[100]_p$ direction. The HAADF-STEM image, known as the so-called Z contrast image, shows a contrast that is roughly proportional to the square of the atomic number [27,28]. The dark intensity contrast and the integrated profile (Fig. 2b) indicate the depletion of La in the core of the stacking fault layer due to La being the heaviest atom in LLTO. Besides, a much brighter intensity contrast of the La-poor columns at the termination layer in the two adjacent domains (Fig. 2a) suggests the segregation of La atoms besides the stacking fault layer. Atomic resolution electron energy loss spectroscopy (EELS) mappings (Fig. 2c) show that O element homogeneously distributed across the stacking fault. The weaker La signals are observed at the center of the stacking fault layer, while two adjacent Ti layers arise at both sides of the La layer. Fig. 2d and e show the EELS spectra of La-M and Ti-L edges collected from the stacking fault layer and neighboring intact lattice regions (labeled with different colors in Fig. 2d), respectively. The change of La- $M_{4,5}$ intensities between the stacking fault (zone 2) and bulk regions (zone 1 and zone 3) shows the deficiency of La in the stacking fault layer, consistent with the HAADF result. The HAADF image in Fig. 2c shows that the Ti columns in zone 2 have slightly less bright contrast as compared to those in zones 1 or 3. The result is indicative of a smaller columnar occupancy of Ti, i.e. the formation of a small amount of Ti vacancies (Ti-missing), in zone 2. In comparison, it should be noted that the smaller difference between the intensity of Ti-L spectra obtained from zone 2 and those obtained from neighboring regions should be caused by the beam broadening effect when collecting the signals. The formation of the Ti vacancies is expected to compensate for the excess positive charge caused by the local La segregation.

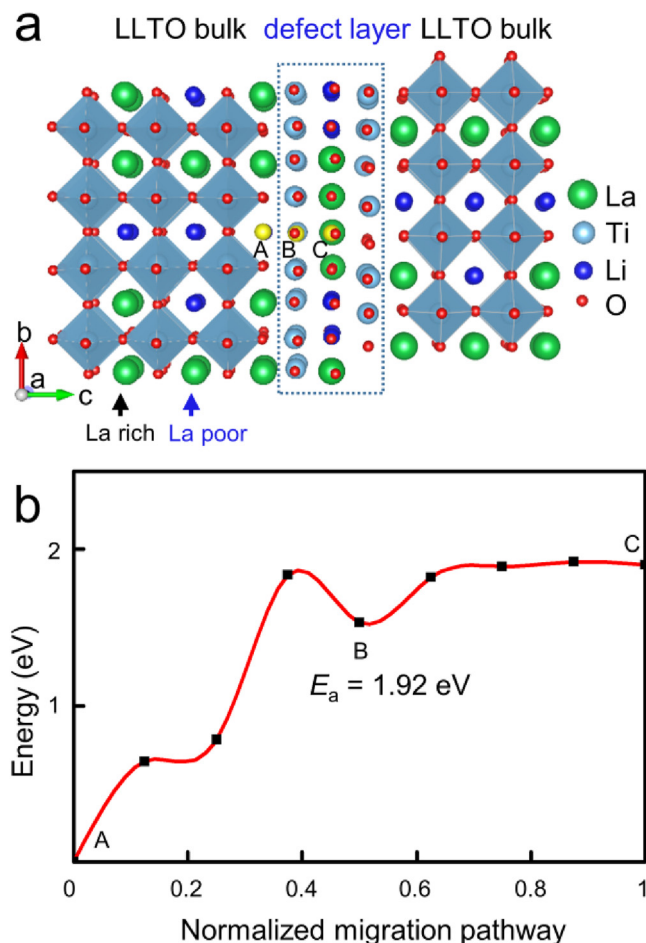


Fig. 3. First-principles calculation of Li-ion transport through the stacking fault layer. (a) Atom structure model of a stacking fault used for the first-principles calculation based on the HAADF-STEM observation. Three yellow-colored Li atoms were used to show the Li-ion migration pathway. (b) The calculated activation energy (E_a) for the Li-ion migration energy through the stacking fault. HAADF, high-angle annular dark field; STEM, scanning transmission electron microscopy.

To investigate the influence of the stacking fault layer on ionic conductivity, the relationship between individual stacking fault and Li-ion migration must be understood first. Based on the structural and chemical analysis above, we constructed the atomic model of the stacking fault for first-principles calculations (Fig. 3a). In such a model, the lattice of the right domain was glided by $1/2[110]_p$ to that of the left side. We assumed a hopping mechanism for Li-ion migration across the defect layer. The three yellow marked Li atom in Fig. 3a indicated the starting point (a), middle point (b), and ending point (c) positions, respectively. Our calculation for such a Li-ion migration pathway produces activation energy of 1.92 eV using the nudged elastic band method. Compared with the migration energy of 0.19 eV for Li-ion diffuse through the La-poor layer in bulk LLTO [22], this high E_a indicates that the defect layers act as blocking layers to Li-ion migration. In other words, Li-ion transport through the defect layers should be forbidden. As these Li-ion-blocking defect layers form enclosed loops, the enclosed volumes surrounded by defect layers are thus isolated from the bulk LLTO and can hardly contribute to the overall Li-ion transport. Therefore, the enclosed volumes surrounded by defect layers should have a negative effect on the overall Li-ion conductivity, similar to pores in ceramics. If future strategies to minimize the density of the defect layers can be developed, further improvement of the overall Li-ion conductivity could be expected.

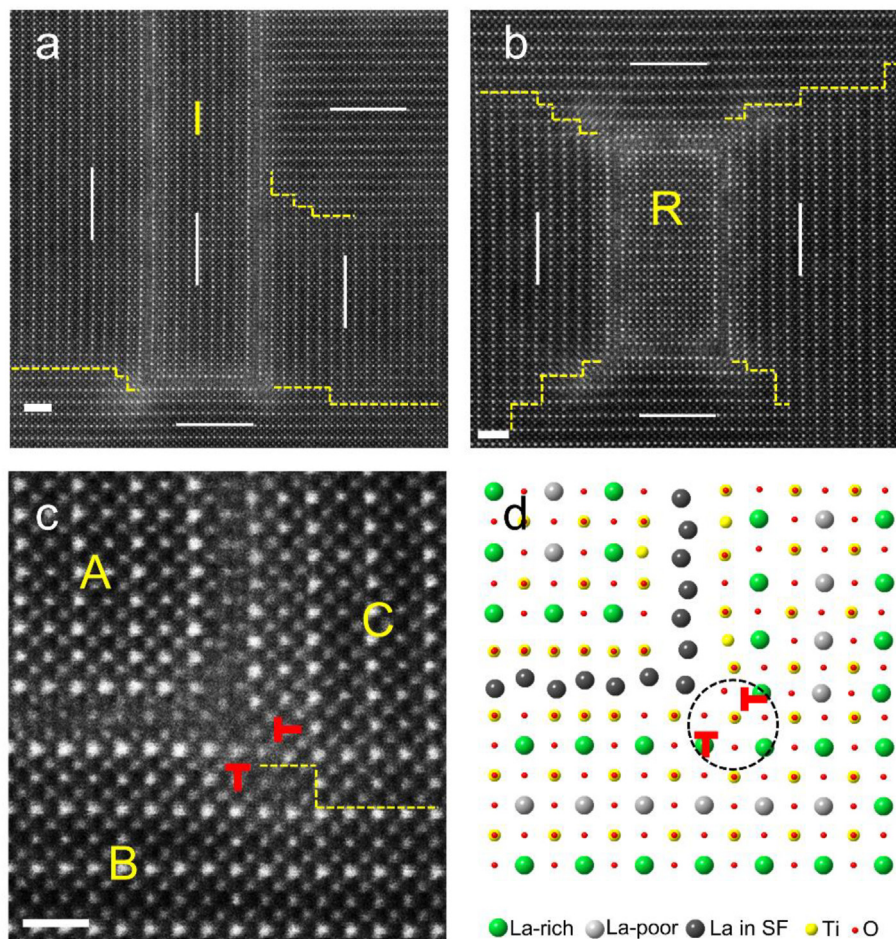


Fig. 4. Corners are formed by stacking faults with dislocation pinning. LAADF images of (a) I loop and (b) R loop. (c) LAADF image of a corner with a 90° DB and a pair of partial dislocations. (d) The corresponding schematic image of (c). White short lines are used to indicate the (001)_p planes of different domains, and yellow dashed lines show that 90° DBs are mostly observed at corners. The scale bars are 2 nm and 1 nm for (a), (b), and (c), respectively. LAADF, low-angle annular dark field; DB, domain boundary.

It's essential to understand the formation mechanism of the stacking faults for improving the overall Li-ion conductivity in LLTO. Fig. 4a and b show the atomic scale LAADF images of the I loop and R loop along [100]_p direction, respectively. It is obvious, in addition to the stacking fault layers, the local unit cells around each corner of both the loops show uniformly brighter intensity contrast than the domain interior. The result suggests a stronger lattice distortion (i.e. stronger lattice strain field) in the corner regions. Fig. 4c and d shows the HAADF image and corresponding schematic atomic structure of the corner formed by stacking faults. Interestingly, a pair of 90°-oriented partial dislocations (indicated by red T) is observed at each corner of the two defect layer loops. Migration of stacking faults is usually accompanied by two partial dislocations, which control the length of stacking faults through gliding [29]. When two 90°-oriented partial dislocations meet and get pinned at corners, the two stacking faults are fixed and reserved during the phase transition. To compensate for the lattice mismatch originating from the partial dislocations, there should be other corners formed at the termination of stacking faults. Thus, the enclosed loops are created in this way.

Previous studies in the famous YBaCuO perovskites system show that 90°-oriented domains were formed during the cubic to

tetragonal transformation [30]. It has been shown that LLTO compounds have a cubic crystal symmetry at high sintering temperatures above 1,200 °C [15–17]. Therefore, it is reasonable to speculate that the domain structure in LLTO is formed as a result of degraded phase transition from cubic phase to tetragonal or orthorhombic phases. The atomic resolution visualization of the enclosed loop structure provides novel insights into the domain growth and the formation of stacking faults in LLTO (Fig. 5). At high temperatures, LLTO exhibits a perovskite cubic phase in which cations (Li, La, and vacancies) are randomly distributed among the A-site positions. During the cooling process, degrading phase transition occurs, which leads to cation ordering in alternate (001)_p planes, resulting in the La-rich layers and La-poor layers. Then the domain nuclei of the degraded LLTO phase are formed randomly within the cubic LLTO crystal interior. Along with the domain growth, interfaces between domains are formed as follows (Fig. 5b): (i) 90° DBs are formed when two domains encounter with different (001)_p orientation and no lattice mismatch to each other; (ii) APBs are generated when two domains with [001]_p lattice mismatch come across; (iii) stacking fault layers are formed between the domains with a lattice glide of $1/2\langle 110 \rangle_p$. The domain growth is accompanied by the creation and migration of dislocations. When a pair of

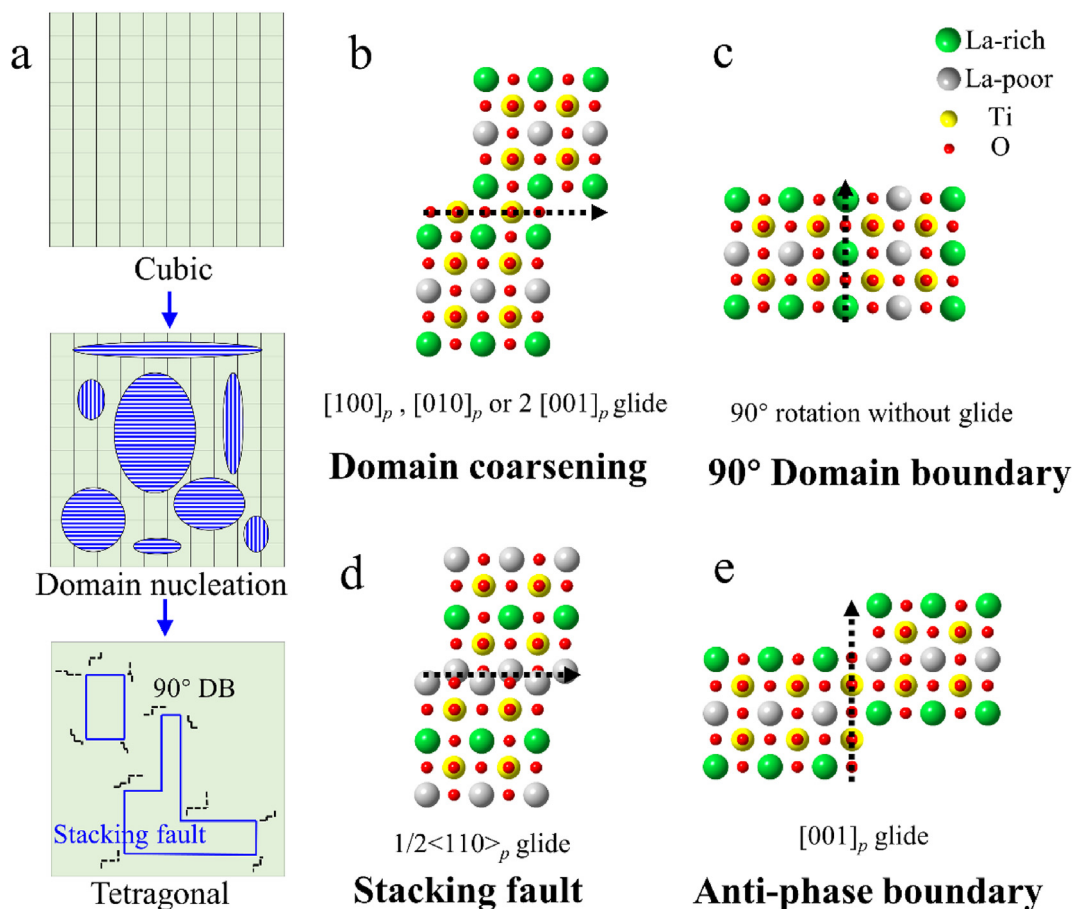


Fig. 5. The formation of domain boundaries and stacking faults enclosed loops. (a) Illustration of domain growth during phase transition. Two domains encountered with different orientation and lattice glide result in (b) domain coarsening, (c) 90° domain boundary, (d) stacking fault, and (e) anti-phase boundary.

90°-oriented partial dislocations meet, default layer loops are hence formed.

3. Conclusion

In summary, based on STEM/EELS analysis, a unique type of intrinsic stacking faults was frequently observed in crystalline LLTO. The stacking faults were found to form enclosed loops associated with segregation La atoms at both sides of the stacking fault layer. First-principles calculations show that the stacking fault layers are supposed to deteriorate the ionic conductivity of this material. In addition, we proposed a kinetic microstructure evolution mechanism, as a result of high-temperature phase transition, to illustrate the domain growth and its relation to the formation of stacking faults. These results unravel the fundamental understanding of intrinsic defects in LLTO, providing guidelines to develop novel SSEs with improved ionic conductivity.

Credit author statements

Shang Peng: Conceptualization, Data Curation, Formal analysis, Investigation, Writing-original draft, Writing-review & editing. **Yongjin Chen:** Formal analysis, Writing-original draft, Writing-review & editing. **Boya Wang:** Data Curation, Investigation, Writing-review & editing. **Xuefeng Zhou:** Data Curation, Investigation, Writing-review & editing. **Haijun Yu:** Data Curation, Investigation, Writing-review & editing. **Jianbo Wang:** Supervision,

Resources, Funding acquisition, Writing-review & editing. **Wenge Yang:** Supervision, Resources, Funding acquisition, Writing-review & editing. **Xiang Gao:** Conceptualization, Data Curation, Formal analysis, Supervision, Resources, Funding acquisition, Writing-review & editing.

Declaration of competing interest

The authors declare that they have no known competing financial interests or personal relationships that could have appeared to influence the work reported in this paper.

Acknowledgments

This work was supported by the National Natural Science Foundation of China (U2030206, U1930401, 22075003, 1210041120, 51527801, 52071237, 12074290, 51871169, 51671148, 11674251, 51601132), the Natural Science Foundation of Jiangsu Province (BK20191187), the Fundamental Research Funds for the Central Universities (2042019kf0190), the Science and Technology Program of Shenzhen (JCYJ20190808150407522), and the China Postdoctoral Science Foundation (2019M652685).

Appendix A. Supplementary data

Supplementary data to this article can be found online at <https://doi.org/10.1016/j.mtener.2021.100912>.

References

- [1] J.B. Goodenough, Rechargeable batteries: challenges old and new, *J. Solid State Electrochem.* 16 (2012) 2019–2029, <https://doi.org/10.1007/s10008-012-1751-2>.
- [2] Z. Zhang, Y. Shao, B. Lotsch, Y.S. Hu, H. Li, J. Janek, L.F. Nazar, C.W. Nan, J. Maier, M. Armand, L. Chen, New horizons for inorganic solid state ion conductors, *Energy Environ. Sci.* 11 (2018) 1945–1976, <https://doi.org/10.1039/c8ee01053f>.
- [3] A. Manthiram, X. Yu, S. Wang, Lithium battery chemistries enabled by solid-state electrolytes, *Nat. Rev. Mater.* 2 (2017) 1–16, <https://doi.org/10.1038/natrevmats.2016.103>.
- [4] J. Janek, W.G. Zeier, A solid future for battery development, *Nat. Energy.* 1 (2016) 1–4, <https://doi.org/10.1038/nenergy.2016.141>.
- [5] C. Yada, A. Ohmori, K. Ide, H. Yamasaki, T. Kato, T. Saito, F. Sagane, Y. Iriyama, Dielectric modification of 5V-class cathodes for high-voltage all-solid-state lithium batteries, *Adv. Energy Mater.* 4 (2014) 1–5, <https://doi.org/10.1002/aenm.201301416>.
- [6] C.-Y. Huang, Y.-T. Tseng, H.-Y. Lo, J.-K. Chang, W.-W. Wu, In situ atomic scale investigation of $\text{Li}_7\text{La}_3\text{Zr}_2\text{O}_{12}$ -based Li^+ -conducting solid electrolyte during calcination growth, *Nano Energy* 71 (2020) 104625, <https://doi.org/10.1016/j.nanoen.2020.104625>.
- [7] S. Stramare, V. Thangadurai, W. Weppner, Lithium lanthanum titanates: a review, *Chem. Mater.* 15 (2003) 3974–3990, <https://doi.org/10.1021/cm0300516>.
- [8] Y. Inaguma, C. Lique, M. Itoh, T. Nakamura, T. Uchida, H. Ikuta, M. Wakihara, High ionic conductivity in lithium lanthanum titanate, *Solid State Commun.* 86 (1993) 689–693, [https://doi.org/10.1016/0038-1098\(93\)90841-A](https://doi.org/10.1016/0038-1098(93)90841-A).
- [9] D. Qian, B. Xu, H.M. Cho, T. Hatsukade, K.J. Carroll, Y.S. Meng, Lithium lanthanum titanium oxides: a fast ionic conductive coating for lithium-ion battery cathodes, *Chem. Mater.* 24 (2012) 2744–2751, <https://doi.org/10.1021/cm300929r>.
- [10] Y. Inaguma, T. Katsumata, M. Itoh, Y. Morii, Crystal structure of a lithium ion-conducting perovskite $\text{La}_{2/3-x}\text{Li}_x\text{TiO}_3$ ($x = 0.05$), *J. Solid State Chem.* 166 (2002) 67–72, <https://doi.org/10.1006/jssc.2002.9560>.
- [11] H. Geng, J. Lan, A. Mei, Y. Lin, C.W. Nan, Effect of sintering temperature on microstructure and transport properties of $\text{Li}_{3x}\text{La}_{2/3-x}\text{TiO}_3$ with different lithium contents, *Electrochim. Acta* 56 (2011) 3406–3414, <https://doi.org/10.1016/j.electacta.2010.06.031>.
- [12] M. Catti, Ion mobility pathways of the Li^+ conductor $\text{Li}_{0.125}\text{La}_{0.625}\text{TiO}_3$ by Ab initio simulations, *J. Phys. Chem. C* 112 (2008) 11068–11074, <https://doi.org/10.1021/jp803345y>.
- [13] K. Kishida, K. Goto, H. Inui, Electron diffraction of ABX_3 perovskites with both layered ordering of A cations and tilting of BX_6 octahedra, *Acta Crystallogr. B* 65 (2009) 405–415, <https://doi.org/10.1107/S0108768109016243>.
- [14] T. Tsurui, T. Katsumata, Y. Inaguma, Direct observations of La ordering and domain structures in $\text{La}_{0.61}\text{Li}_{0.17}\text{TiO}_3$ by high resolution electron microscopy, *Philos. Mag. A* 89 (2009) 843–852, <https://doi.org/10.1080/14786430902740711>.
- [15] Y. Harada, H. Watanabe, J. Kuwano, Y. Saito, Lithium ion conductivity of A-site deficient perovskite solid solutions, *J. Power Sources* 81–82 (1999) 777–781, [https://doi.org/10.1016/S0378-7753\(99\)00105-6](https://doi.org/10.1016/S0378-7753(99)00105-6).
- [16] J. Ibarra, A. Vázquez, C. León, J. Santamaría, L.M. Torres-Martínez, J. Sanz, Influence of composition on the structure and conductivity of the fast ionic conductors $\text{La}_{2/3-x}\text{Li}_x\text{TiO}_3$ ($0.03 \leq x \leq 0.167$), *Solid State Ionics* 134 (2000) 219–228, [https://doi.org/10.1016/S0167-2738\(00\)00761-X](https://doi.org/10.1016/S0167-2738(00)00761-X).
- [17] O. Bohnke, H. Duroy, J.L. Fourquet, S. Ronchetti, D. Mazza, In search of the cubic phase of the Li^+ -ion-conducting perovskite $\text{La}_{2/3-x}\text{Li}_x\text{TiO}_3$: structure and properties of quenched and in situ heated samples, *Solid State Ionics* 149 (2002) 217–226, [https://doi.org/10.1016/S0167-2738\(02\)00142-X](https://doi.org/10.1016/S0167-2738(02)00142-X).
- [18] Y. Inaguma, M. Nakashima, A rechargeable lithium-air battery using a lithium ion-conducting lanthanum lithium titanate ceramics as an electrolyte separator, *J. Power Sources* 228 (2013) 250–255, <https://doi.org/10.1016/j.jpowsour.2012.11.098>.
- [19] S. Sasano, R. Ishikawa, K. Kawahara, T. Kimura, Y.H. Ikuhara, N. Shibata, Y. Ikuhara, Grain boundary Li -ion conductivity in $(\text{Li}_{0.33}\text{La}_{0.56})\text{TiO}_3$ polycrystal, *Appl. Phys. Lett.* 116 (2020) 1–4, <https://doi.org/10.1063/1.5141396>.
- [20] T. Salkus, E. Kazakevicius, A. Kežionis, A.F. Orliukas, J.C. Badot, O. Bohnke, Determination of the non-Arrhenius behaviour of the bulk conductivity of fast ionic conductors LLTO at high temperature, *Solid State Ionics* 188 (2011) 69–72, <https://doi.org/10.1016/j.ssi.2010.09.005>.
- [21] X. Gao, C.A.J. Fisher, T. Kimura, Y.H. Ikuhara, A. Kuwabara, H. Moriwake, H. Oki, T. Tojigamori, K. Kohama, Y. Ikuhara, Domain boundary structures in lanthanum lithium titanates, *J. Mater. Chem. A* 2 (2014) 843–852, <https://doi.org/10.1039/c3ta13726k>.
- [22] H. Moriwake, X. Gao, A. Kuwabara, C.A.J. Fisher, T. Kimura, Y.H.Y. Ikuhara, K. Kohama, T. Tojigamori, Y.H.Y. Ikuhara, Domain boundaries and their influence on Li migration in solid-state electrolyte $(\text{La}, \text{Li})\text{TiO}_3$, *J. Power Sources* 276 (2015) 203–207, <https://doi.org/10.1016/j.jpowsour.2014.11.139>.
- [23] F. Zhu, M.S. Islam, L. Zhou, Z. Gu, T. Liu, X. Wang, J. Luo, C.W. Nan, Y. Mo, C. Ma, Single-atom-layer traps in a solid electrolyte for lithium batteries, *Nat. Commun.* 11 (2020) 1–9, <https://doi.org/10.1038/s41467-020-15544-x>.
- [24] C. Ma, K. Chen, C. Liang, C.W. Nan, R. Ishikawa, K. More, M. Chi, Atomic-scale origin of the large grain-boundary resistance in perovskite Li -ion-conducting solid electrolytes, *Energy Environ. Sci.* 7 (2014) 1638–1642, <https://doi.org/10.1039/c4ee00382a>.
- [25] K. Shen, R. He, Y. Wang, C. Zhao, H. Chen, Atomistic insights into the role of grain boundary in ionic conductivity of polycrystalline solid-state electrolytes, *J. Phys. Chem. C* 124 (2020) 26241–26248, <https://doi.org/10.1021/acs.jpcc.0c07328>.
- [26] P.J. Phillips, M. De Graef, L. Kovarik, A. Agrawal, W. Windl, M.J. Mills, Atomic-resolution defect contrast in low angle annular dark-field STEM, *Ultramicroscopy* 116 (2012) 47–55, <https://doi.org/10.1016/j.ultramicro.2012.03.013>.
- [27] S.J. Pennycook, Z-contrast stem for materials science, *Ultramicroscopy* 30 (1989) 58–69, [https://doi.org/10.1016/0304-3991\(89\)90173-3](https://doi.org/10.1016/0304-3991(89)90173-3).
- [28] Y. Chen, B. Zhang, Y. Zhang, H. Wu, K. Peng, H. Yang, Q. Zhang, X. Liu, Y. Chai, X. Lu, G. Wang, Z. Zhang, J. He, X. Han, X. Zhou, Atomic-scale visualization and quantification of configurational entropy in relation to thermal conductivity: a proof-of-principle study in $\text{t-GeSb}_2\text{Te}_4$, *Adv. Sci.* 8 (2021) 1–10, <https://doi.org/10.1002/advs.202002051>.
- [29] C. He, Y. Zhang, C.Q. Liu, Y. Yue, H.W. Chen, J.F. Nie, Unexpected partial dislocations within stacking faults in a cold deformed Mg-Bi alloy, *Acta Mater.* 188 (2020) 328–343, <https://doi.org/10.1016/j.actamat.2020.02.010>.
- [30] G. Lacayo, G. Kästner, R. Herrmann, Twin to tweed transition in $\text{YBa}_2\text{Cu}_3\text{O}_{7-\delta}$ by substitution of Al for Cu, *Phys. C Supercond.* 192 (1992) 207–214, [https://doi.org/10.1016/0921-4534\(92\)90762-2](https://doi.org/10.1016/0921-4534(92)90762-2).